World Scientific
www.worldscientific.com

Correlation of image textures of a polarization feature parameter and the microstructures of liver fibrosis tissues

Yue Yao*, Jiachen Wan*, Fengdi Zhang*, Yang Dong*,
Lihong Chen[‡,§,¶,∥] and Hui Ma[*,†,**]

*Tsinghua Shenzhen International Graduate School
Shenzhen Key Laboratory for Minimal Invasive Medical Technologies
Institute of Optical Imaging and Sensing, Shenzhen 518055, P. R. China

†Tsinghua University, Department of Physics
Beijing 100084, P. R. China

‡Fujian Medical University, Department of Pathology and
Institute of Oncology, School of Basic Medical Sciences
Fuzhou 350014, P. R. China

§Fujian Medical University, Diagnostic Pathology Center
Fuzhou 350014, P. R. China

¶Fujian Medical University, Mengchao Hepatobiliary Hospital
Fuzhou 350014, P. R. China
∥drlhchen@sina.com
**mahui@tsinghua.edu.cn

Mueller matrix imaging is emerging for the quantitative characterization of pathological microstructures and is especially sensitive to fibrous structures. Liver fibrosis is a characteristic of many types of chronic liver diseases. The clinical diagnosis of liver fibrosis requires time-consuming multiple staining processes that specifically target on fibrous structures. The staining proficiency of technicians and the subjective visualization of pathologists may bring inconsistency to clinical diagnosis. Mueller matrix imaging can reduce the multiple staining processes and provide quantitative diagnostic indicators to characterize liver fibrosis tissues. In this study, a fiber-sensitive polarization feature parameter (PFP) was derived through the forward sequential feature selection (SFS) and linear discriminant analysis (LDA) to target on the identification of fibrous structures. Then, the Pearson correlation coefficients and the statistical T-tests between the fiber-sensitive PFP image textures and the liver fibrosis tissues were calculated. The results show the gray level run length matrix (GLRLM)-based run entropy that measures the

[∥,**]Corresponding authors.

heterogeneity of the PFP image was most correlated to the changes of liver fibrosis tissues at four stages with a Pearson correlation of 0.6919. The results also indicate the highest Pearson correlation of 0.9996 was achieved through the linear regression predictions of the combination of the PFP image textures. This study demonstrates the potential of deriving a fiber-sensitive PFP to reduce the multiple staining process and provide textures-based quantitative diagnostic indicators for the staging of liver fibrosis.

1. Introduction

Liver cirrhosis ranks as the 11th leading cause of death and 15th cause of morbidity worldwide in 2016. Chronic liver diseases lead to 1.32 million deaths worldwide in 2017. Liver fibrosis refers to the formation of fibrous structures when the liver repairs damaged or inflamed liver tissues. It is a characteristic of many types of chronic liver diseases and severe liver fibrosis often leads to cirrhosis.[1,2] The clinical diagnoses of liver fibrosis at different stages require multiple staining processes including hematoxylin and eosin (H&E) staining, Masson's trichrome staining that specifically targets fibrous structures, and Gordon and Sweet's silver staining that specifically targets reticular fibers.[3–5] The multiple staining processes are time-consuming and the difference in staining proficiency of technicians may make contributions to inconsistent diagnostic outcomes.

Mueller matrix imaging is an emerging label-free, noninvasive technique that contains abundant sub-wavelength scale histopathological microstructures and has promising application potentials in clinical early detection, diagnosis, and prognosis of various cancerous diseases.[6–14] Previous research indicates Mueller matrix imaging is especially sensitive to fibrous structures of pathological tissues. Dong *et al.* used Mueller matrix polar decomposition (MMPD) derived linear retardance parameter δ and its corresponding orientation angle parameter θ and Mueller matrix transformation (MMT) derived linear birefringence-related parameters x and t to quantitatively characterize the density and orientation of fibrous structures in breast ductal carcinoma tissues.[15] Laude-Boulesteix *et al.* presented a liquid-crystal modulators-based polarimetric imaging system to study the optical properties including the diattenuation, retardance and polarizance of a 10-μm thick Picrosirius Red stained liver cirrhosis slide over a wide spectral range.[16] Wang *et al.* analyzed the average values of MMPD parameter δ and MMT parameter t of four sections of 8-μm thick nonstained and dewaxed liver fibrosis tissues to demonstrate Mueller matrix imaging is sensitive to the increase of fibrous structures in liver fibrosis tissues from stage F1 to stage F4.[17] Lee *et al.* also pointed out variations in pathological tissue cut thickness will lead to variations in optical path length, which will affect the measurements of polarization and depolarization of a tissue sample. Therefore, they proposed several approaches combined with Beer–Lambert law to mitigate the impact of tissue thickness fluctuations and provide more reliable diagnostics of histological changes such as fibrosis, inflammation and cancer.[18]

This study is dedicated to presenting a liver fibrosis diagnostic procedure using polarimetric Mueller matrix microscopy to quantitatively characterize the liver fibrosis tissues at four stages. This polarimetric diagnostic procedure will help to reduce the time-consuming multiple staining processes and provide quantitative diagnostic indicators to overcome the limitations resulting from the experience-oriented diagnostic procedures. In this study, a fiber-sensitive polarization feature parameter (PFP) was derived from 25 polarization basis parameters (PBPs) through the combination of forward sequential feature selection (SFS) and linear discriminant analysis (LDA) to target on the quantitative characterization of liver fibrosis tissues at four stages.[19–21] The fiber-sensitive PFP is a linear combination of 12 selected significant PBPs. After obtaining the fiber-sensitive PFP, a correlation study between the image textures of the PFP and the liver fibrosis tissues was performed to explore the possibility of developing polarization textures-based liver fibrosis diagnostic indicators that can facilitate the quantitative diagnosis of liver fibrosis.

2. Materials and Methods

2.1. *Liver fibrosis tissues and experimental setup*

The 38 H&E-stained liver fibrosis slides (4-μm thick) used in this study were acquired from 38 patients from Mengchao Hepatobiliary Hospital. Among the 38 slides, a total of 10 slides, 10 slides, nine slides and nine slides were diagnosed as stage S1, stage S2, stage S3 and stage S4 by the Scheuer system, respectively.[22] For each liver fibrosis slide, one region of interest (ROI) that represents the typical liver fibrosis histological features as shown in Fig. 1 was labeled by an experienced pathologist to acquire PBP images under an objective lens of 4× resolution. This study was approved by the Ethics Committee of the Mengchao Hepatobiliary Hospital.

The schematic of the dual division of focal plane (DoFP) polarimeters-based full Mueller matrix microscope (DoFPs-MMM) used for fast full Mueller matrix imaging was shown in Fig. 2(a).[23] The DoFPs-MMM is modified from a commercial transmission microscope (L2050, Guangzhou LISS Optical Instrument Co., Ltd., China) by adding a polarization state generator (PSG) and a polarization state analyzer (PSA). The PSG is composed of a fixed-angle linear polarizer (P1) and a rotatable zero-order quarter-wave plate (R1). The PSA is composed of two 16-bit DoFP polarimeters (PHX050S-PC, Lucid Vision Labs Inc., Canada), a 50:50 nonpolarized beam splitter prism (CCM1-BS013/M, Thorlabs Inc., USA), and a fixed-angle phase retarder (R2). During the experiment, the light from the LED is modulated by the PSG and then passes through the liver fibrosis sample.
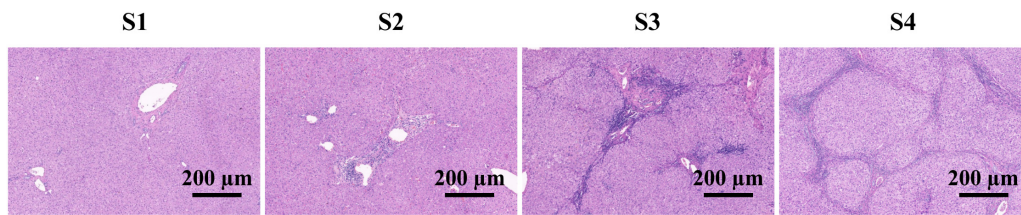

Fig. 1.   The labeled ROI of the 4-μm thick H&E-stained liver fibrosis tissues at stages of S1, S2, S3 and S4 under an objective lens of 4× resolution.
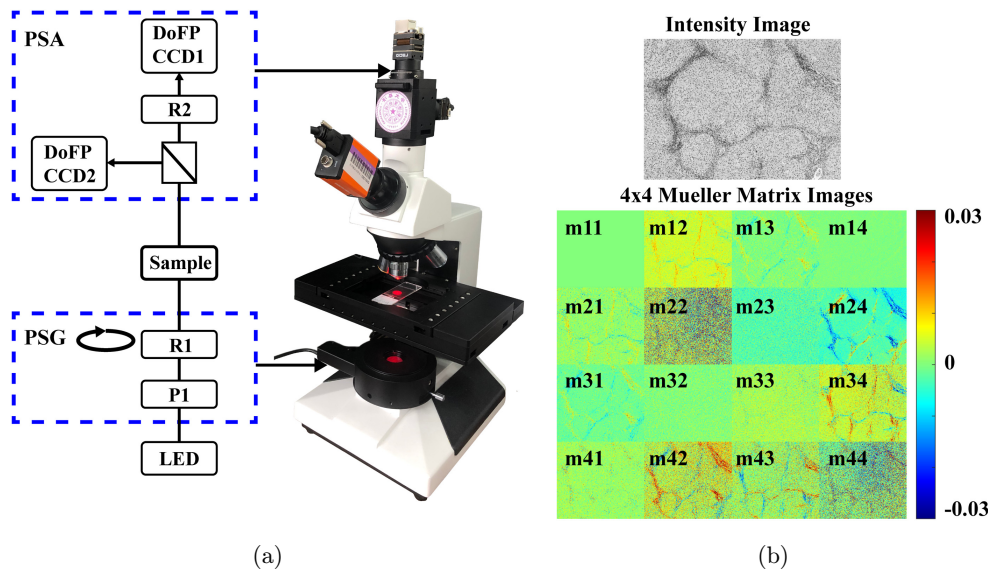

Fig. 2.   (a) Schematic of the dual DoFP polarimeters-based full Mueller matrix microscope. P1: a fixed-angle linear polarizer; R1: a rotatable zero-order quarter-wave plate; R2: a fixed-angle phase retarder; PSG: a polarization state generator; PSA: a polarization state analyzer; Light source: LED (633 nm, $\Delta\lambda = 20$ nm). (b) An example of intensity image and 4×4 Mueller matrix image of a liver fibrosis sample. The values of m_{11} were set to 0 and the values of m_{22}, m_{33} and m_{44} were subtracted by 1 only for display purposes.

The scattered light from the sample then passes through the objective lens and detected by the two DoFP polarimeters of the PSA.

To acquire the 4×4 Mueller matrix as shown in Fig. 2(b), the PSG will generate four independent polarization states by rotating the fast axis of R1 to four angles of $\pm 45°$ and $\pm 19.6°$. The PSA will measure four linear polarization channels including $90°$, $45°$, $135°$ and $0°$ in a single shot by the two DoFP polarimeters. To enable the measurement of four linear polarization channels in a single shot, the DoFP polarimeter adds a pixelated micro-polarizer array (MPA) in front of an ordinary CCD sensor to form a super-pixel that contains four adjacent pixels with different polarization orientations for each pixel. The DoFPs-MMM measured Mueller matrices have very small average root mean square errors (RMSEs) of less than 0.01 for standard samples including a linear polarizer and a wave plate of $92.62°$ retardance at $633\,\mathrm{nm}$. Detailed information on the DoFP polarimeters-based full Mueller matrix microscope was published in Ref. 23.[23,24]

2.2. *Derivation of the PFP*

In Mueller matrix imaging, the Mueller matrix contains full polarization information of a pathological sample, but the absence of explicit explanations of specific tissue microstructures from individual Mueller matrix elements leads to the derivation of polarization parameters with more clear physical meanings. Li *et al.* reviewed various polarization parameters derived from different physical methods to provide quantitative characterizations of pathological samples.[25,26] In this study, a total of 25 polarization parameters derived from different physical methods were used as PBPs to derive a fiber-sensitive PFP that contains combined histological information and targets the identification of fibrous structures of liver fibrosis tissues. A fiber-sensitive PFP is a linear combination of selected significant PBPs. The 25 PBPs used include MMPD parameters δ, D, Δ and R[27–29]; MMT parameters P_L, D_L, q_L and r_L[26]; MMT parameters b, β, $|\boldsymbol{B}|$, $\|\boldsymbol{B}\|$, t_1 and CD[25]; Degree of linear polarization parameter LDOP[25]; and Cloude decomposition parameters $\lambda_{1\sim4}$, P_1, P_2, P_3, P_Δ, $S(\boldsymbol{H})$ and PI.[6,25,26,30–34]

The fiber-sensitive PFP derivation procedures involve three steps: (1) pathologist labels the fibrous and nonfibrous pixels of liver fibrosis tissues on H&E images; (2) image registration is performed between the H&E image and the 25 PBP images for each sample to acquire the input fibrous and nonfibrous pixels and training labels of the 25 PBPs. A total of 45,000 fibrous pixels (2500 pixels each ROI) and 45,000 nonfibrous pixels (2500 pixels each ROI) were randomly sampled from 18 liver fibrosis tissue ROIs (S3 and S4) for the machine learning process; (3) and the derivation of a fiber-sensitive PFP through the combination of machine learning-based forward SFS and LDA. The LDA is a supervised dimensionality reduction technique that also can perform classification simultaneously. It focuses on finding a feature subspace that maximizes the separation between fibrous and nonfibrous pixels. For the combination of the forward SFS and LDA, the forward SFS sequentially chooses the best PBP to add based on the highest five-fold cross-validation scores of the LDA classifier. The combined forward SFS and LDA can be used to look for a fiber-sensitive PFP, which is a linear combination of a selected number of significant PBPs that has the highest classification accuracy to identify the fibrous and nonfibrous pixels.[19–21]

2.3. *Correlation analysis of image textures of the PFP*

Liver fibrosis tissues at different stages show different histological structures. A correlation study between the image textures of the fiber-sensitive PFP and the liver fibrosis histological structures can provide texture-based quantitative diagnostic indicators that can be used alone or combined with other clinical indicators for the staging and further grading of liver fibrosis tissues. To perform the correlation study, first, the image textures of the fiber-sensitive PFP for each liver fibrosis sample were calculated. These image textures include 25 gray level co-occurrence matrix (GLCM)-based features and 16 gray level run length matrix (GLRLM)-based features.[35] The names and calculation equations of the 41 image textures were listed in Ref. 35.[35] Then, the Pearson correlation coefficient that measures the strength of a linear correlation between a PFP image texture and the liver fibrosis tissues at four stages was calculated to find the PFP image textures that are most associated with the changes in liver fibrosis structures.[19,36]

Besides, the statistical T-test was also calculated for the PFP image textures with the top five highest Pearson correlation coefficients to study whether these image textures are statistically significant to distinguish the liver fibrosis tissues at four stages.[37,38]

3. Results and Discussion

3.1. *The derived fiber-sensitive PFP for liver fibrosis tissues*

In this study, the combination of forward SFS and LDA derived a fiber-sensitive PFP by selecting 12 significant PBPs from a total of 25 PBPs based on the highest five-fold cross-validation scores of the LDA to classify the two-class fibrous and no-fibrous pixels. This fiber-sensitive PFP is a linear combination of the 12 significant PBPs that maximize the separation of the fibrous and nonfibrous pixels with the highest five-fold cross-validation classification accuracy of 86.54% and weighting coefficients shown in Fig. 3. The 12 significant PBPs as shown in Fig. 3 include Muller matrix transformation (MMT) parameters β, $|\boldsymbol{B}|$, CD, P_L and r_L, degree of linear polarization parameter LDOP, Cloude decomposition parameters λ_1, λ_3 and $S(\boldsymbol{H})$, and MMPD parameters Δ, δ and R.[25] The MMT parameter β is related to circular retardance. Parameter $|\boldsymbol{B}|$ is the determinant of Mueller matrix central 2×2 blocks and is affected by the linear diattenuation and linear retardance. Parameter CD is the degree of circular dichroism anisotropy.[39] Parameter P_L is the linear polarizance and parameter r_L is related to the linear birefringence. Parameter LDOP represents the degree of linear polarization. For the Cloude decomposition parameters, λ_1 and λ_3 are the eigenvalues of the covariance matrix of Mueller matrix $\boldsymbol{H}(\boldsymbol{M})$.[40] Parameter $S(\boldsymbol{H})$ is the polarization entropy.[31] For the MMPD parameters, Δ is the degree of overall

depolarization, δ is related to linear retardance and R is the total retardance that includes both effects of linear retardance and circular retardance.[28]

Among the 12 significant PBPs, some of them are correlated with similar physical meanings such as the depolarization Δ and the LDOP. However, the combination of the forward SFS and LDA selected this linear combination of 12 significant PBPs from a total of 25 PBPs due to their highest classification accuracy. Besides, the LDA weighting coefficients for the depolarization Δ and the LDOP were 0.527 and -0.847, respectively, which indicate they made different contributions to classifying the fibrous and nonfibrous pixels. Therefore, in this study, the results indicate that even though some PBPs such as the depolarization Δ and the LDOP were correlated, they may not be completely substitutable.

Figure 4 shows the examples of selected PBPs P_L and r_L, and the derived fiber-sensitive PFP for liver fibrosis tissues from stages S1–S4. Previous research indicates the linear polarizance parameter P_L is sensitive to cell nucleus structures. The linear birefringence-related parameter r_L is sensitive to fibrous structures.[41,42] Figure 4 also shows parameter r_L is more sensitive to liver fibrous structures than parameter P_L. The derived fiber-sensitive PFP is the linear combination of diattenuation, retardance and depolarization-related parameters and encodes more comprehensive liver fibrosis cellular and fibrous structures. Figure 4 indicates the derived fiber-sensitive PFP highlights more fibrous pixels than the linear polarizance parameter P_L and the linear birefringence-related parameter r_L, especially at stages S3 and S4 that contain more fibrous structures.

3.2. *Correlation of image textures of fiber-sensitive PFP and liver fibrosis*

The Pearson product–moment correlation coefficient measures the strength of a linear association
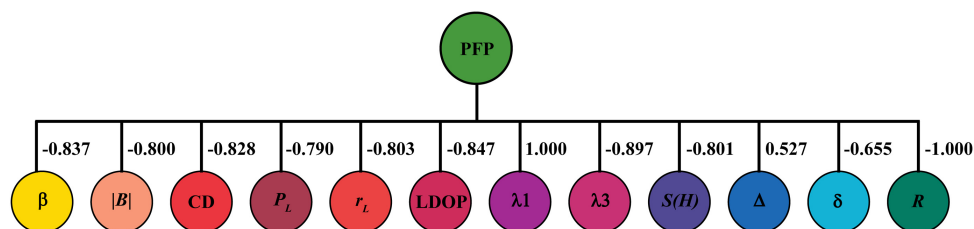

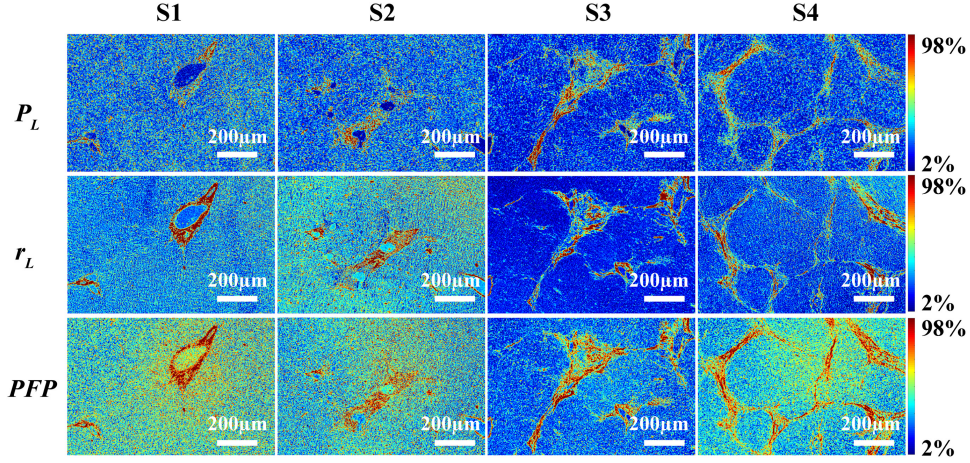Fig. 3. The fiber-sensitive PFP derived from a linear combination of 12 significant PBPs.

Fig. 4. Imaging results of the selected significant PBPs P_L and D_L, and the derived fiber sensitive PFP for liver fibrosis tissues at stages S1, S2, S3 and S4. The image color bar ranges from the 2nd percentile to the 98th percentile of that image.

between the data of two variables. A Pearson correlation coefficient that equals 0 indicates there is no association between the two variables. A Pearson correlation coefficient that is greater than 0 indicates a positive association and a Pearson correlation coefficient that is less than 0 indicates a negative association. The Pearson correlation coefficient will be close to $+1$ (positive correlation) or -1 (negative correlation) for a stronger correlation between two variables.[19,36] In this study, the Pearson correlation coefficients between the image textures of the fiber-sensitive PFP and the four stages of liver fibrosis tissues were calculated. The image textures include 25 GLCM-based features and 16 GLRLM-based features.[35] The detailed image texture names and calculation equations are listed in Ref. 35.[35] In this study, the statistical T-test was also calculated for the PFP image texture to study

whether this image texture is statistically significant to distinguish the liver fibrosis tissues at four stages.

Table 1 listed the top five image textures with the highest Pearson correlation coefficients among the 41 GLCM and GLRLM-based features in descending order. The GLRLM-based run entropy measures the randomness of the distributions of run lengths and gray level values. The PFP image with a larger run entropy indicates it has texture patterns with more heterogeneity. The GLRLM-based run entropy of the PFP image has the highest Pearson correlation coefficient of 0.6919. This result indicates that image heterogeneity has the largest association with the changes in liver fibrosis tissues at different stages. The gray level nonuniformity and normalized gray level nonuniformity that measure the similarity of gray-level intensity values in the fiber-sensitive PFP images have Pearson

Table 1. Pearson correlation and statistical T-test of PFP image textures.

	Pearson correlation		p-value		
	Top 5 PFP textures	Value	S1–S2	S2–S3	S3–S4
GLRLM	Run entropy	0.6919	0.1717	0.1756	0.0151
GLRLM	Gray level nonuniformity	0.6659	0.1938	0.2203	0.0191
GLRLM	Normalized gray level nonuniformity	0.6617	0.2020	0.2313	0.0193
GLCM	Information correlation 1	0.6611	0.2078	0.2106	0.0261
GLRLM	SRHGLE	0.6326	0.0057	0.2779	0.0709
	PFP textures with linear regression	Value	S1–S2	S2–S3	S3–S4
	Combination of top 5 PFP textures	0.7400	0.0898	0.1429	0.0048
	Combination of top 10 PFP textures	0.7923	0.0049	0.2322	0.0014
	Combination of top 20 PFP textures	0.8959	≈ 0	0.1538	0.0002
	Combination of all 41 PFP textures	0.9996	≈ 0	≈ 0	≈ 0

correlation coefficients of 0.6659 and 0.6617, respectively. The GLCM-based information correlation 1 that measures the complexity of the image using mutual information has a Pearson correlation coefficient of 0.6611.[43] The GLRLM-based short run high gray level emphasis (SRHGLE) that measures the joint distribution of short run lengths with high gray-level values has a Pearson correlation coefficient of 0.6326. These results indicate the heterogeneity, similarity, complexity and distribution of high gray-level values with short run lengths of the fiber-sensitive PFP images are most correlated to the changes in liver fibrosis structures from stage S1 to stage S4.

Table 1 also shows the *p*-values of the statistical *T*-tests for liver fibrosis tissues between stages S1 and S2, S2 and S3, and S3 and S4. The results demonstrate the GLRLM-based run entropy, gray level nonuniformity and normalized gray level nonuniformity, and GLCM-based information correlation 1 showed statistically significant differences for liver fibrosis tissues at stages S3 and S4 with *p*-values equal to 0.0151, 0.0191, 0.0193 and 0.0261, respectively, which means only one image texture that either describes the heterogeneity, similarity or complexity is required to distinguish the liver fibrosis tissues at stages S3 and S4 with a statistically significant difference. However, these image textures do not show significant differences for liver fibrosis tissues between S1 and S2, and S2 and S3 with *p*-values all greater than 0.05. The GLCM-based SRHGLE shows a significant difference for

liver fibrosis tissues at S1 and S2 with a *p*-value equal to 0.0057. However, this texture does not show significant differences for liver fibrosis tissues at other stages.

The individual image textures only show a statistically significant difference between stages S1 and S2 or S3 and S4. A single image texture is not able to separate the liver fibrosis tissues at stages S2 and S3. Therefore, linear regression was used to fit the combination of PFP image textures based on the ranking of Pearson correlation coefficients. The combinations of top 5, top 10, top 20 and 41 PFP image textures were chosen for fitting a linear regression model that minimizes the residual sum of squares between the observed targets and the targets predicted by the linear approximation.[44,45] Table 1 also illustrated the Pearson correlation coefficients and statistical *p*-values for the predictions of the linear regression model with the combinations of 5, 10, 20 and 41 PFP image textures, respectively.

Figure 5 shows the linear regression predictions of liver fibrosis tissues at four stages by using combinations of the fiber-sensitive PFP image textures. For the predictions through the top five PFP image textures as shown in Fig. 5(a), the Pearson correlation coefficient was 0.7400 and this combination only shows a statistically significant difference to separate liver fibrosis tissues at S3 and S4. For the predictions through the top 10 PFP image textures as shown in Fig. 5(b), the Pearson correlation coefficient was 0.7923 and this
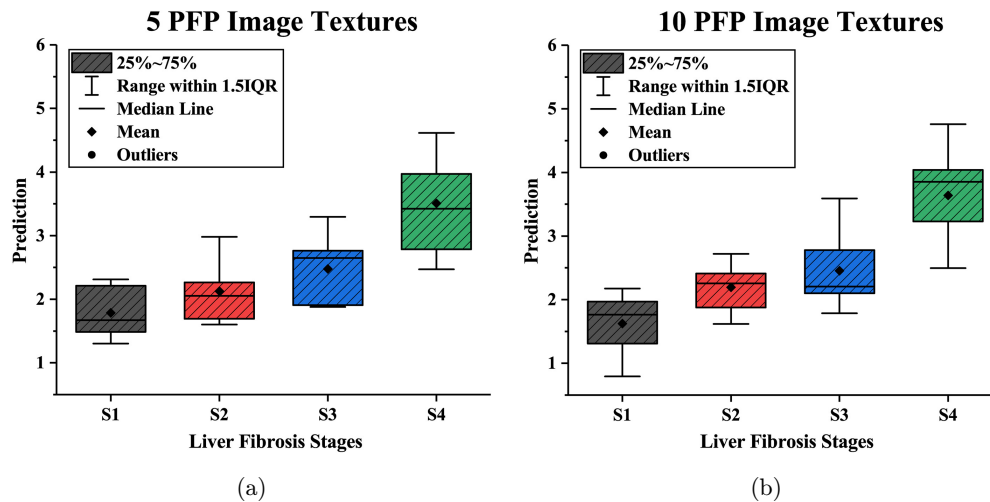

Fig. 5. Linear regression predictions of liver fibrosis tissues at four stages by using a combination of the fiber-sensitive PFP image textures. (a) Predictions through top five PFP image textures. (b) Predictions through top 10 PFP image textures. (c) Predictions through top 20 PFP image textures. (d) Predictions through all 41 PFP image textures.
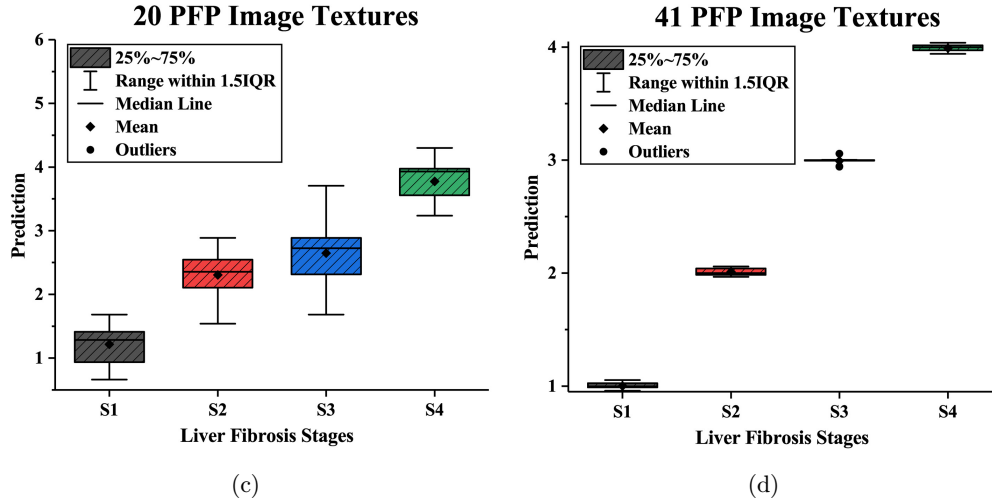
20 PFP Image Textures

(c)

41 PFP Image Textures

(d)

Fig. 5. (*Continued*)

combination demonstrates a statistically significant difference to separate liver fibrosis tissues between S1 and S2, and between S3 and S4. For the predictions through the top 20 PFP image textures as shown in Fig. 5(c), the Pearson correlation coefficient was 0.8959 and this combination shows better separations for stages S1 and S2, and stages S3 and S4. However, it still does not show a significant difference between S2 and S3. This result indicates the PFP image patterns for liver fibrosis tissues at S2 and S3 have large overlaps and are the most difficult to separate with fewer PFP image textures. Figure 5(d) shows the predictions using all of the 41 calculated image textures. For this combination, the Pearson correlation coefficient was 0.9996 and the predictions can separate all of the four stages of liver fibrosis tissue samples with a statistically significant difference. The results in Table 1 demonstrate that the heterogeneity, similarity and complexity of the fiber-sensitive PFP images have the largest Pearson correlations with the changes in liver fibrosis structures from S1 to S4. The results in Fig. 5 demonstrate the image textures of the fiber-sensitive PFP have the potential to develop textures-based quantitative diagnostic indicators that can be used alone or combined with other clinical indicators for the staging of liver fibrosis tissues and further study of fibrous microstructures in liver cancerous tissues for diagnostic and prognostic applications.

4. Conclusions

In conclusion, Mueller matrix imaging is an emerging label-free, noninvasive technique that is especially sensitive to the fibrous microstructures of pathological samples. In this study, a fiber-sensitive PFP was derived from 25 PBPs by using the combination of forward SFS and LDA to target on the identification of fibrous structures. The fiber-sensitive PFP is a linear combination of 12 PBPs and highlights more fibrous structures than a single PBP such as the linear polarizance parameter P_L and the linear birefringence-related parameter r_L, especially for liver fibrosis tissues at stages S3 and S4 that contains more fibrous structures. After obtaining the fiber-sensitive PFP, the Pearson correlation coefficient that measures the strength of a linear association between the fiber-sensitive PFP image texture and the liver fibrosis tissues at different stages was calculated for a total of 41 GLCM and GLRLM-based image textures. The results indicate the PFP image texture with the largest Pearson correlation of 0.6919 was the GLRLM-based run entropy that measures the heterogeneity of the image. This image texture shows a statistically significant difference for liver fibrosis tissues at stages S3 and S4 and can be used as quantitative indicators to distinguish S3 and S4. However, this single image texture does not show a significant difference to separate S1 and S2, and S2 and S3. Therefore, the linear regression was used to fit the combination of PFP image textures based on the

ranking of Pearson correlation coefficients. The linear regression predictions for the combinations of top 5, 10, 20 and 41 image textures show increasing Pearson correlation coefficients of 0.7400, 0.7923, 0.8959 and 0.9996, respectively. The combination of 41 PFP image textures with the largest Pearson correlation coefficient of 0.9996 can quantitatively identify all of the liver fibrosis samples at four stages. This study demonstrates the potential of deriving fiber-sensitive PFPs to provide textures-based quantitative diagnostic indicators that can be used alone or combined with other immunohisto-chemical or clinical indicators for the staging of liver fibrosis and further study of fibrous-related liver cancer microenvironments for diagnostic and prognostic applications.

Conflicts of Interest

The authors have no conflicts of interest relevant to this article.

Acknowledgments

References

1. S. Cheemerla, M. Balakrishnan, "Global epidemiology of chronic liver disease," *Clin. Liver Dis.* **17**, 365 (2021).

2. S. K. Asrani, H. Devarbhavi, J. Eaton, P. S. Kamath, "Burden of liver diseases in the world," *J. Hepatol.* **70**, 151–171 (2019).

3. A. H. Fischer, K. A. Jacobson, J. Rose, R. Zeller, "Hematoxylin and eosin staining of tissue and cell sections," *Cold Spring Harb. Protoc.* **2008**, pdb-prot4986 (2008).

4. N. C. Foot, "The Masson trichrome staining methods in routine laboratory use," *Stain Technol.* **8**, 101–110 (1933).

5. H. Gordon, H. H. Sweets Jr., "A simple method for the silver impregnation of reticulum," *Am. J. Pathol.* **12**, 545 (1936).

6. H. He, R. Liao, N. Zeng, P. Li, Z. Chen, X. Liu, H. Ma, "Mueller matrix polarimetry — an emerging new tool for characterizing the microstructural feature of complex biological specimen," *J. Lightw. Technol.* **37**, 2534–2548 (2019).

7. C. He, H. He, J. Chang, B. Chen, H. Ma, M. J. Booth, "Polarisation optics for biomedical and clinical applications: A review," *Light: Sci. Appl.* **10**, 1–20 (2021).

8. J. Qi, D. S. Elson, "A high definition Mueller polarimetric endoscope for tissue characterisation," *Sci. Rep.* **6**, 1–11 (2016).

9. J. Qi, D. S. Elson, "Mueller polarimetric imaging for surgical and diagnostic applications: A review," *J. Biophoton.* **10**, 950–982 (2017).

10. T. Liu, M. Lu, B. Chen, Q. Zhong, J. Li, H. He, H. Mao, H. Ma, "Distinguishing structural features between Crohns disease and gastrointestinal luminal tuberculosis using Mueller matrix derived parameters," *J. Biophoton.* **12**, e201900151 (2019).

11. P. Schucht, H. R. Lee, H. M. Mezouar, E. Hewer, A. Raabe, M. Murek, I. Zubak, J. Goldberg, E. Kövari, A. Pierangelo, T. Novikova, "Visualization of white matter fiber tracts of brain tissue sections with wide-field imaging Mueller polarimetry," *IEEE Trans. Med. Imaging* **39**, 4376–4382 (2020).

12. H. R. Lee, I. Saytashev, V. N. Du Le, M. Mahendroo, J. Ramella-Roman, T. Novikova, "Mueller matrix imaging for collagen scoring in mice model of pregnancy," *Sci. Rep.* **11**, 1–12 (2021).

13. H. He, N. Zeng, D. Li, R. Liao, H. Ma, "Quantitative Mueller matrix polarimetry techniques for biological tissues," *J. Innov. Opt. Health Sci.* **5**, 1250017 (2012).

14. Y. Huang, A. Hou, J. Wang, Y. Yao, W. Miao, X. Tian, J. Yu, C. Li, H. Ma, Y. Fan, "Identification of serous ovarian tumors based on polarization imaging and correlation analysis with clinicopathological features," *J. Innov. Opt. Health Sci.* 2241002 (2022).

15. Y. Dong, J. Qi, H. He, C. He, S. Liu, J. Wu, D. S. Elson, H. Ma, "Quantitatively characterizing the microstructural features of breast ductal carcinoma tissues in different progression stages by Mueller matrix microscope," *Biomed. Opt. Express* **8**, 3643–3655 (2017).

16. B. Laude-Boulesteix, A. De Martino, B. Drévillon, L. Schwartz, "Mueller polarimetric imaging system with liquid crystals," *Appl. Opt.* **43**, 2824–2832 (2004).

17. Y. Wang, H. He, J. Chang, C. He, S. Liu, M. Li, N. Zeng, J. Wu, H. Ma, "Mueller matrix microscope: A quantitative tool to facilitate detections and fibrosis scorings of liver cirrhosis and cancer tissues," *J. Biomed. Opt.* **21**, 071112 (2016).

18. H. R. Lee, P. Li, T. S. H. Yoo, C. Lotz, F. K. Groeber-Becker, S. Dembski, E. Garcia-Caurel, R. Ossikovski, H. Ma, T. Novikova, "Digital histology with Mueller microscopy: How to mitigate an impact of tissue cut thickness fluctuations," *J. Biomed. Opt.* **24**, 076004 (2019).

19. F. Pedregosa, G. Varoquaux, A. Gramfort, V. Michel, B. Thirion, O. Grisel, M. Blondel,

P. Prettenhofer, R. Weiss, V. Dubourg, "Scikit-learn: Machine learning in Python," *J. Mach. Learn. Res.* **12**, 2825–2830 (2011).

20. A. Géron, *Hands-on Machine Learning with Scikit-Learn, Keras, and TensorFlow: Concepts, Tools, and Techniques to Build Intelligent Systems* (O'Reilly Media, Sebastopol, CA, USA, 2019), p. 235.

21. F. J. Ferri, P. Pudil, M. Hatef, J. Kittler, "Comparative study of techniques for large-scale feature selection," in *Machine Intelligence and Pattern Recognition* (Elsevier, North-Holland, 1994), pp. 403–413.

22. N. D. Theise, "Liver biopsy assessment in chronic viral hepatitis: A personal, practical approach," *Mod. Pathol.* **20**, S3–S14 (2007).

23. T. Huang, R. Meng, J. Qi, Y. Liu, X. Wang, Y. Chen, R. Liao, H. Ma, "Fast Mueller matrix microscope based on dual DoFP polarimeters," *Opt. Lett.* **46**, 1676–1679 (2021).

24. B. M. Ratliff, C. F. LaCasse, J. S. Tyo, "Interpolation strategies for reducing IFOV artifacts in microgrid polarimeter imagery," *Opt. Express* **17**, 9112–9125 (2009).

25. P. Li, Y. Dong, J. Wan, H. He, T. Aziz, H. Ma, "Polaromics: Deriving polarization parameters from a Mueller matrix for quantitative characterization of biomedical specimen," *J. Phys. D: Appl. Phys.* (2021).

26. P. Li, D. Lv, H. He, H. Ma, "Separating azimuthal orientation dependence in polarization measurements of anisotropic media," *Opt. Express* **26**, 3791–3800 (2018).

27. S.-Y. Lu, R. A. Chipman, "Interpretation of Mueller matrices based on polar decomposition," *J. Opt. Soc. Am. A* **13**, 1106–1113 (1996).

28. S. Manhas, M. K. Swami, P. Buddhiwant, N. Ghosh, P. K. Gupta, K. Singh, "Mueller matrix approach for determination of optical rotation in chiral turbid media in backscattering geometry," *Opt. Express* **14**, 190–202 (2006).

29. N. Ghosh, M. F. G. Wood, I. A. Vitkin, "Mueller matrix decomposition for extraction of individual polarization parameters from complex turbid media exhibiting multiple scattering, optical activity, and linear birefringence," *J. Biomed. Opt.* **13**, 044036 (2008).

30. Y. Dong, J. Wan, X. Wang, J.-H. Xue, J. Zou, H. He, P. Li, A. Hou, H. Ma, "A polarization-imaging-based machine learning framework for quantitative pathological diagnosis of cervical precancerous lesions," *IEEE Trans. Med. Imaging* **40**, 3728–3738 (2021).

31. R. Barakat, "Polarization entropy transfer and relative polarization entropy," *Opt. Commun.* **123**, 443–448 (1996).

32. A. Tariq, P. Li, D. Chen, D. Lv, H. Ma, "Physically realizable space for the purity-depolarization plane for polarized light scattering media," *Phys. Rev. Lett.* **119**, 033202 (2017).

33. J. J. Gil, E. Bernabeu, "Depolarization and polarization indices of an optical system," *Opt. Acta: Int. J. Opt.* **33**, 185–189 (1986).

34. A. Hou, X. Wang, Y. Fan, W. Miao, Y. Dong, X. Tian, J. Zou, H. Ma, "Polarimetry feature parameter deriving from Mueller matrix imaging and auto-diagnostic significance to distinguish HSIL and CSCC," *J. Innov. Opt. Health Sci.* **15**, 2142008 (2022).

35. A. Zwanenburg, S. Leger, M. Vallières, S. Löck, "Image biomarker standardisation initiative," arXiv:1612.07003.

36. C. R. Harris, K. J. Millman, S. J. van der Walt, R. Gommers, P. Virtanen, D. Cournapeau, E. Wieser, J. Taylor, S. Berg, N. J. Smith, "Array programming with NumPy," *Nature* **585**, 357–362 (2020).

37. D. Semenick, "Tests and measurements: The *T*-test," *Strength Cond. J.* **12**, 36–37 (1990).

38. T. K. Kim, "*T*-test as a parametric statistic," *Korean J. Anesthesiol.* **68**, 540 (2015).

39. O. Arteaga, E. Garcia-Caurel, R. Ossikovski, "Anisotropy coefficients of a Mueller matrix," *J. Opt. Soc. Am. A* **28**, 548–553 (2011).

40. S. Nechayev, R. Barczyk, U. Mick, P. Banzer, "Substrate-induced chirality in an individual nanostructure," *ACS Photon.* **6**, 1876–1881 (2019).

41. M. Sun, H. He, N. Zeng, E. Du, Y. Guo, S. Liu, J. Wu, Y. He, H. Ma, "Characterizing the microstructures of biological tissues using Mueller matrix and transformed polarization parameters," *Biomed. Opt. Express* **5**, 4223–4234 (2014).

42. Y. Yao, M. Zuo, Y. Dong, L. Shi, Y. Zhu, L. Si, X. Ye, H. Ma, "Polarization imaging feature characterization of different endometrium phases by machine learning," *OSA Contin.* **4**, 1776–1791 (2021).

43. J. J. M. Van Griethuysen, A. Fedorov, C. Parmar, A. Hosny, N. Aucoin, V. Narayan, R. G. H. Beets-Tan, J.-C. Fillion-Robin, S. Pieper, H. J. W. L. Aerts, "Computational radiomics system to decode the radiographic phenotype," *Cancer Res.* **77**, e104–e107 (2017).

44. D. C. Montgomery, E. A. Peck, G. G. Vining, *Introduction to Linear Regression Analysis* (John Wiley & Sons, Hoboken, New Jersey, USA, 2021), pp. 12–35.

45. G. A. F. Seber, A. J. Lee, *Linear Regression Analysis* (John Wiley & Sons, 2012).